Glancing-Angle X-ray Absorption Spectroscopy of Corroded Borosilicate Glass Surfaces Containing Uranium

G. N. Greaves,*,† N. T. Barrett,‡ G. M. Antonini,§ F. R. Thornley,∥ B. T. M. Willis,⊥ and A. Steel†

Contribution from the SERC Daresbury Laboratory, Warrington WA4 4AD, UK, Department of Pure and Applied Chemistry, University of Strathclyde, Glasgow G1 1XL, UK, Dipartimento di Fisica, Università di Modena, Via Campi 213/a, Modena 41100, Italy, Department of Pure and Applied Physics, University of Strathclyde, Glasgow G4 0NG, UK, and Chemical Crystallography Laboratory, 9 Parks Road, Oxford OX1 3PD, UK. *Received June 21, 1988*

Abstract: The local atomic structure surrounding uranium in borosilicate glass has been investigated by fluorescence X-ray absorption spectroscopy. By employing angles of incidence either side of the critical angle for total external reflection, surface and near-surface structure can be distinguished. The results of leaching in water at 100 °C have been examined in detail. Wet and dried glass surfaces can be differentiated. Analysis of glancing-angle spectra demonstrates that uranium occupies a uranyl-like environment that hydrates as leaching progresses. Uranyl complexing occurs in a planar geometry. The initial corrosion process can be readily understood by using the modified random network model for glass structure, which predicts diffusion of cations and water taking place via percolation pathways through the network. Following extended corrosion treatment, evidence for the formation of hydrated uranyl silicates at the surface has been found.

1. Introduction

The structural chemistry underlying the aqueous corrosion of oxide glasses has been extensively studied in recent years by a wide variety of techniques: weight loss,[1,2] leachate analysis,[3,4] pH-stat,[3,5] solution conductivity,[6,7] RBS,[3,6] nuclear reaction analysis,[8-10] IRR,[11] FTIR,[12] and Raman[6,13] spectroscopies, SEM,[14] electron microprobe,[4] SIMS,[15] NPBSIMS,[16] and XPS.[17] These are analytical methods for the most part and give no direct structural information about the ways in which the glass surface is modified as corrosion progresses. Moreover, many of the techniques employed to date require a high-vacuum sample environment, precluding in situ experiments. Because water is absorbed into the surface of the glass during corrosion, subsequent evacuation of the specimen necessarily alters the composition of the leached layer, thereby affecting the overall structure at the surface. Furthermore, depth profiling of composition variations is often achieved destructively by successive etching or sputtering of the glass surface. Glancing-angle X-ray absorption spectroscopy suffers from none of these disadvantages. The local atomic environment of a particular element in the glass can be measured directly, and by employing the geometry of total external reflection, structure at the surface can be revealed. Furthermore, the use of hard X-rays enables experiments to be conducted in air under natural conditions. Finally, by varying the angle of incidence of the incident X-rays, changes in the structure can be recorded nondestructively as a function of depth.

1.1. Glancing-Angle X-ray Absorption Spectroscopy. X-ray absorption spectroscopy[18] has been used for several years to elucidate the bulk atomic structure of oxide glasses.[19,20] The extended X-ray absorption fine structure (EXAFS) enables the pair distribution functions of both glass formers (e.g., SiO_2) and network modifiers (e.g., Na_2O, CaO, etc.) to be differentiated.[19] The shape and position of the absorption edges—the X-ray absorption near-edge structure or XANES—can be used to identify the local symmetry and oxidation state of metal ions like iron,[20] or in this case, uranium.[21] However, the standard transmission or fluorescence geometries employed to measure EXAFS and XANES[22] are not sensitive to structure at the surface. Surface sensitivity, though, can be achieved by the glancing-angle geometry illustrated in the inset to Figure 1. It is well-known[23,24] that for a monochromatic X-ray beam incident on a flat surface there exists a well-defined angle of incidence, φ_c, below which the angle of refraction, φ', is zero and total external reflectance takes place. This is because the index of refraction, n, for most materials at X-ray energies is less than 1. In particular, $\varphi_c = (2\delta)^{1/2}$, where $1 - \delta$ is the real part of n. In practical units

$$\varphi_c \sim 20\rho^{1/2}/E \text{ (mrad)} \quad (1)$$

† SERC Daresbury Laboratory.
‡ Dept. of Pure and Applied Chemistry, University of Strathclyde.
§ Università di Modena.
∥ Dept. of Pure and Applied Physics, University of Strathclyde.
⊥ Chemical Crystallography Laboratory, Oxford.

(1) Matej, J.; Hlaváč, J. *Silikaty (Prague)* **1967**, *11*, 3.
(2) Day, D. H.; Hughes, A. E.; Leake, J. W.; Marples, J. A.; Marsh, G. P.; Rae, J.; Wade, B. O. *Rep. Prog. Phys.* **1985**, *48*, 101.
(3) Bunker, B. C.; Arnold, G. N.; Beauchamp, E. K.; Day, D. D. *J. Non-Cryst. Solids* **1983**, *58*, 295.
(4) Schreiber, H. D.; Balazs, G. B.; Solberg, T. N. *Phys. Chem. Glasses* **1985**, *26*, 35.
(5) Pederson, L. R. *Phys. Chem. Glasses* **1987**, *28*, 17.
(6) Sales, B. C.; White, C. W.; Begun, G. M.; Boatner, L. A. *J. Non-Cryst. Solids* **1984**, *67*, 245.
(7) Sales, B. C.; Boatner, L. A. *J. Non-Cryst. Solids* **1986**, *79*, 83.
(8) Pederson, L. R.; Baer, D. R.; McVay, G. L.; Engelhard, M. H. *J. Non-Cryst. Solids* **1986**, *86*, 369.
(9) Lanford, W. A.; Davis, K.; Lamarche, P.; Lawsen, T.; Groleau, R.; Doremus, R. H. *J. Non-Cryst. Solids* **1979**, *33*, 249.
(10) Arnold, G. W.; Peercy, P. S. *J. Non-Cryst. Solids* **1980**, *41*, 359.
(11) Zellmer, L. A.; White, W. B. In *Scientific Basis for Nuclear Waste Management VIII*; Jantzen, C. M., Stone, J. A., Ewing, R. C., Eds.; MRS: Pittsburgh, PA, 1985; p 73.
(12) Ferris, K. E.; Pederson, L. R. *Phys. Chem. Glasses* **1988**, *29*, 9.
(13) Exarhos, G. J.; Conway, W. E. *J. Non-Cryst. Solids* **1983**, *55*, 445.
(14) Schiewer, E.; Lutze, W.; Boatner, L. A.; Sales, B. C. In *Scientific Basis for Nuclear Waste Management IX*; Werme, L., Ed.; MRS: Pittsburgh, PA, 1986; p 231.
(15) Smets, B. M. J.; Lommen, T. P. A. *Phys. Chem. Glasses* **1982**, *23*, 83.
(16) Richter, T.; Frischat, G. H.; Borchardt, G.; Sherrer, S. *Phys. Chem. Glasses* **1985**, *26*, 208. Richter, T.; Frischat, G. H.; Borchardt, G.; Scherrer, S.; Weber, S. *Mikrochim. Acta* **1985**, *Suppl. 11*, 163.
(17) Manara, A.; Lanza, F.; Ceccone, G.; Della Mea, G.; Salvagno, G. In *Scientific Basis for Nuclear Waste Management VIII*; Jantzen, C. M., Stone, J. A., Ewing, R. C., Eds.; MRS: Pittsburgh, PA, 1985; p 85.
(18) Sayers, D. E.; Lytle, F. W.; Stern, E. A. *Phys. Rev. Lett.* **1971**, *27*, 1204.
(19) Greaves, G. N.; Fontaine, A.; Lagarde, P.; Raoux, D.; Gurman, S. J. *Nature* **1981**, *293*, 611.
(20) Greaves, G. N. *J. Non-Cryst. Solids* **1985**, *71*, 203.
(21) Petiau, J.; Calas, G.; Petitmaire, D.; Bianconi, A.; Benfatto, M.; Marcelli, A. *Phys. Rev. B* **1986**, *34*, 7350.
(22) Brown, G. S.; Doniach, S. In *Synchrotron Radiation Research*; Winick, H., Doniach, S., Eds.; Plenum: New York, 1980.
(23) Parratt, L. G. *Phys. Rev.* **1954**, *95*, 359.
(24) Vineyard, G. H. *Phys. Rev. B* **1982**, *26*, 4146.

0002-7863/89/1511-4313$01.50/0

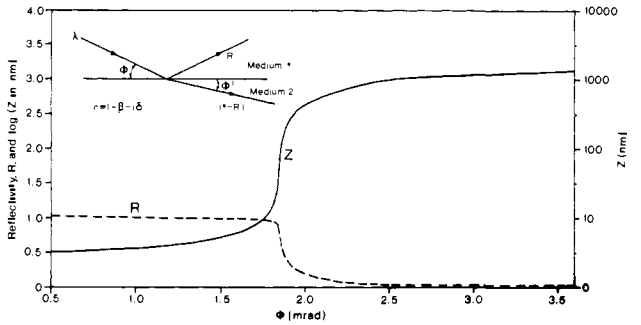

Figure 1. Reflectivity and penetration depth for borosilicate glass doped with uranium for an incident energy at the uranium L_{III} absorption edge. The penetration depth increases from $z_{min} = 31$ Å toward the absorption limit at large φ. The inset shows the geometry for total reflection. A well-collimated, monochromatic X-ray beam is incident at an angle φ with respect to a flat interface. This gives rise to a specularly reflected beam and a refracted beam as indicated. Below the critical angle for total external reflection the angle of refraction $\varphi' = 0$.

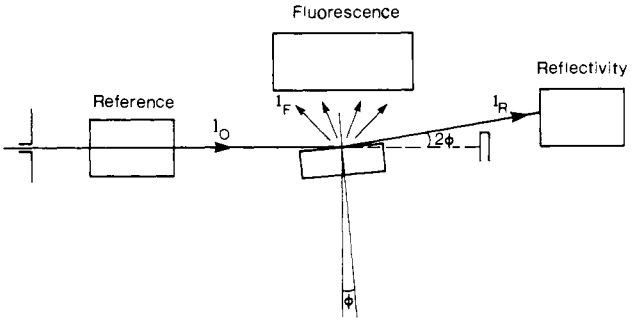

Figure 2. Schematic drawing of the apparatus for fluorescence X-ray absorption spectroscopy at glancing angle. Radiation of energy E is delivered by the monochromator from the synchrotron source. The reference ion chamber detects the incident radiation. I_0 strikes the sample at a glancing angle φ and is specularly reflected at 2φ by the surface. The reflected intensity I_R is detected by a second ion chamber. A beam stop prevents detection of the direct beam. A wide-angle ion chamber is positioned above the sample to detect the fluorescence emission from the sample surface. I_F is recorded as function of incident energy for an energy spectrum scan at a fixed angle of incidence φ.

where ρ (g cm^{-3}) is the density of the material and E (keV) the energy of the X-rays. Application of the Fresnel equations to a two-media interface leads to an expression for the X-ray reflectivity dependent on both the X-ray energy, E, and the angle of incidence, φ. This is illustrated in Figure 1, where the reflectivity calculated for a borosilicate glass at an incident X-ray energy of 17.2 keV is plotted as a function of φ; 17.2 keV is just above the position of the uranium L_{III} absorption edge. Below φ_c total external reflection takes place. At φ_c the reflectivity falls rapidly toward zero. Electromagnetic theory predicts that for $\varphi/\varphi_c \ll 1$ the refracted wave does not penetrate the second medium but remains instead at the surface, propagating parallel to the surface, vibrating in a plane perpendicular to the surface, and coupled to the standing wave generated by the incident and the reflected waves.

The penetration, z, of the X-rays into the second medium is also plotted in Figure 1. z is governed by the damping of this evanescent wave in the direction perpendicular to the interface. As φ decreases, z falls to a minimum, $z_{min} = \lambda/(4\pi\varphi_c)$, given approximately by

$$z_{min} \sim 48/\rho^{1/2}\ (\text{Å}) \qquad (2)$$

For a borosilicate glass and X-rays of 17.2 keV, z_{min} is 31 Å. As φ is increased through φ_c this penetration rapidly increases,[25] approaching the limiting case for $\varphi \gg \varphi_c$

$$z = \sin \varphi/\mu \qquad (3)$$

where μ is the linear absorption coefficient of the material for the incident radiation. For borosilicate glass $z_{max} = 1/\mu = 0.76$ mm at the U L_{III} edge.

Hence, by suitable choice of the angular position of the incident beam surface specific structural information can be obtained by X-ray spectroscopy. This will come from the first few atomic layers for an angle of incidence less than the critical angle, or from a surface region that may be over 1 μm thick in the case of an angle just above the critical angle (see Figure 1).

The X-ray absorption at glancing angles can be measured by using the reflected[26] or the fluorescence[27] signals with the arrangement shown in Figure 2. For dilute samples, Heald, Keller, and Stern[27] have shown that the fluorescence mode gives the more favorable signal-to-noise ratio. In this paper we describe the application of the technique to detect the changing environment of uranium at the surface of a sodium borosilicate glass subjected to progressive aqueous corrosion.

The particular choice of system is related to the problem of nuclear waste disposal where the major limitations on the use of glass for storage is corrosion in an aqueous environment.[2] Preliminary results have already been published.[25] In that study, and in the present work, the uranium was stored in the glass at 0.2 atom %, typical of nuclear waste loading. Work by other groups using X-ray absorption spectroscopy has been performed by measuring specimens in transmission.[21,28] As a result, only bulk structural information is revealed. Moreover, this geometry is restricted to comparatively high concentrations of metal (≥5 atom %). Nonetheless, it has been shown that the uranium environment depends both on the glass composition and on the mode of preparation. The present measurements using fluorescence detection and employing glancing angles were made to examine the structural basis of the chemical resistance of the glass to aqueous attack. The exercise demonstrates the versatility of glancing-angle X-ray absorption spectroscopy for studying problems in corrosion science.

1.2. Uranium in Glass and Glass Corrosion. Uranium exhibits a variety of oxidation states and may exist as U(IV), U(V), or U(VI) in a glass, depending on the redox conditions applying during fusion.[4] The presence of other elements may act as a redox buffer for the uranium oxidation state.[29,30] In a borosilicate melt the diffusing species of uranium has been identified as the complex uranyl ion[31] UO_2^{2+}. This is a distorted octahedron, in its simplest form, with two short axial oxygens and four longer equatorial oxygens. In the solid state the uranyl ion forms layer structures;[32] the exact geometry varies considerably between uranates, hydrates, and silicates (see Table III). X-ray absorption spectroscopy has already been used to determine the bulk oxidation state of, and the local atomic structure around, uranium in oxide glasses.[21,28,33,34] Uranium has been identified as existing in the U(V) or the U(VI) states, the predominant species depending on the oxidation conditions employed in preparation. In addition to the strong U–O correlations, U–U correlations have also been identified,[28] suggesting lineaments of uranyl layers characteristic of crystalline compounds persist in the glassy state.

It is now well-established that the aqueous corrosion of oxide glasses is initiated by the depletion of alkali ions from the surface and the influx of water, culminating in the hydrolysis and sub-

(25) Thornley, F. R.; Barrett, N. T.; Greaves, G. N.; Antonini, G. M. *J. Phys. C* **1986**, *19*, L563.
(26) Martens, P.; Rabe, P. *Phys. Status Solidi A* **1980**, *58*, 415.
(27) Heald, S. M.; Keller, E.; Stern, E. A. *Phys. Lett. A* **1985**, *103*, 155.
(28) Knapp, G. S.; Veal, B. W.; Lam, D. J.; Paulikas, A. P.; Pan, H. K. *Mater. Lett.* **1984**, *2*, 253.
(29) Schreiber, H. D.; Minnix, L. M.; Balazs, G. B.; Carpenter, B. E. *Phys. Chem. Glasses* **1984**, *25*, 1.
(30) Schreiber, H. D.; Carpenter, B. E.; Eckenrode, J. P.; Balazs, G. B. *Phys. Chem. Glasses* **1985**, *26*, 24.
(31) Dunn, T. *J. Non-Cryst. Solids* **1987**, *92*, 1.
(32) Wells, A. F. *Structural Inorganic Chemistry*; Clarendon Press: Oxford, U.K., 1975; p 990.
(33) Antonini, G. M.; Merlini, A.; Thornley, F. R. *Springer Ser. Chem. Phys.* **1984**, *27*, 297.
(34) Petitmaire, D.; Petiau, J.; Calas, G.; Jacquet-Francillon, N. *J. Phys. Colloq.* **1986**, *47*, 849.

sequent dissolution of the glass network.[35-41] The leaching rate (where leaching refers, in general, to the removal of elements from a glass by aqueous corrosion) varies with the temperature of the solution,[4] its pH,[3,42] and not least on the glass composition.[29,30,37] For a simple binary or ternay silicate held at 70 or 80 °C in a closed system for ~1 h, the depletion layer—sometimes called the gel layer—can extend several microns into the glass surface[9,15,36,37] at which stage dissolution is the dominant leaching mechanism. Extensive corrosion results in the saturation of the gel layer and usually leads to the formation of an insoluble—possibly crystalline—surface layer.[4,14,41] This may result, on the one hand, from the precipitation of the least soluble species out of solution,[14] or alternatively, it may recondense out of the gel layer.[4] The corrosion of uranium in borosilicate glass appears to follow the latter course. Although sodium is depleted from the surface, the uranium content is enhanced.[4] The glancing-angle X-ray absorption spectroscopy results that follow add considerable detail to this picture. The gradual hydrolysis of the uranium environment can be detected; the clustering of uranyl groups at the surface and the eventual formation of a surface layer are distinguished.

1.3. Structural Models. The precise diffusion and dissolution processes motivating the aqueous corrosion of silicate glasses are unclear, but the following scheme[35,38] is generally in good qualitative agreement with experiment. The initial dependence of the leaching rate on the square root of the leaching time[1,15,16] points to corrosion being rate-controlled by a diffusion mechanism. Alkalis leave the glass and are replaced by water, resulting in the formation of silanol groups in place of nonbridging oxygen linkages, e.g., Si–O–Na. However, *which* diffusion process is rate-determining is unclear. Also there is contrary evidence as to whether H^+,[5] H_3O^+,[16] or molecular water[43] is active in the interdiffusion. What seems certain is that more water enters the glass than is required simply to replace depleted alkali cations. As corrosion progresses, the leaching rate assumes a linear time dependence[1,5,8] indicating the onset of wholesale dissolution of the glass network, silanol groups being formed from bridging siloxane bonds, i.e., ≡Si—O—Si≡, with the eventual release of silicic acid into solution.[12] The important observation that oxygen uptake in the glass surface is greater than the proton uptake[8] strongly supports the view that considerable recondensation takes place in the depleted layer as leaching continues.

In this paper we will show that the modified random network (MRN) model is particularly useful for depicting the corrosion processes in silicate glasses. This model[20] was proposed to explain the well-defined environment of modifying cations in mixed-oxide glasses. Modifying cations in an MRN form islands in the network, and for stable glass compositions, these become continuous pathways through the glass as shown in Figure 14. The notion of percolation routes for mobile cations is absent in models based on the concepts of Zachariasen.[44] We identify these modifier channels with the transport processes that result in ion exchange and network hydrolysis during aqueous corrosion. In particular, uranium is expected to find itself in close proximity to sodium in sodium borosilicate glass.[28] As such it will encounter, and indeed be active in, the initial ion-exchange process as non-

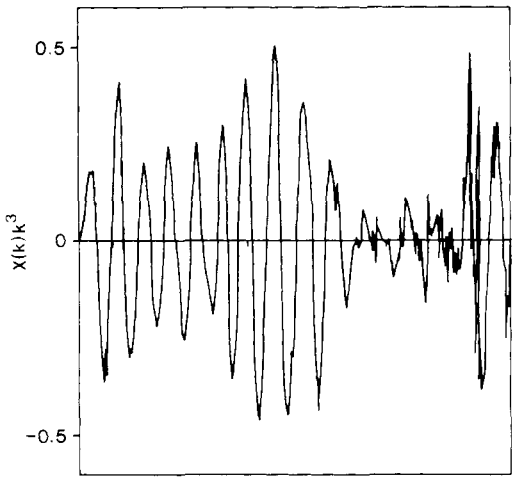

Figure 3. Background-subtracted, k^3-weighted raw EXAFS data for uranium metal. The same spectrum after Fourier filtering the high r components to remove experimental noise and the low r components to remove atomic EXAFS is shown in Figure 4a.

bridging oxygens become protonated. In the later stages of corrosion, as uranium builds up in the gel layer, this cation will provide a useful structural tracer for any recondensation occurring at the surface.

2. Experimental Section

The EXAFS and XANES spectra were recorded by using synchrotron radiation on the wiggler station 9.2 of the Daresbury Synchrotron Radiation Source (SRS). Figure 2 shows schematically the arrangement used to measure the fluorescence and reflectivity. Monochromatic radiation passes through the first ion chamber and strikes the sample at angle φ. The reflected beam is measured by the second ion chamber and the fluroescence emission by a third ion chamber positioned above the sample. The fluoresence ion chamber has a Be window of diameter 96 mm giving a solid angle acceptance of ~3 sr for a typical sample-to-detector distance of ~50 mm. The spectra were recorded at the uranium L_{III} edge (17.16 keV). A Si(220) two-crystal monochromator was used with the second crystal detuned to provide harmonic rejection.[45] Argon gas was used in the I_0 and I_R ion chambers, and Xe in the I_f ion chamber. For the fluorescence detection, filters were not used. The reason for this is that at the high X-ray energies associated with the U L_{III} edge the cross sections for Rayleigh and Compton scattering from the light glass matrix are significantly smaller than the absorption cross section.[46]

The sample alignment was carried out as follows. The monochromator exit slits were closed down to 50 μm to define an incident beam. The sample was aligned relative to the beam in both the transverse and longitudinal senses. The reflectivity was then measured as a function of angle in order to check the calibration of the critical angle φ_c. Once the angular positions for taking the absorption spectra had been determined, the slits before the sample were opened up to accept the extended SRS source height of 300 μm. At 20 m from the source this maximized the incident intensity without significantly degrading the angular resolution. To ensure that the beam was only incident on the sample surface a jaw was positioned to mask the front end of the sample. The angular position was checked for each new sample.

The glass samples were prepared under oxidizing conditions in platinum crucibles from their constiuent oxides at the Stazione Sperimentale del Vetro, Murano, Italy (17.2 Si, 9.2 B, 13.0 Na, 2.1 Al, 0.2 U, 58.3 O in atom %). The fusion was carried out at 1200 °C for 1 h; homogeneity was ensured by remelting three times. Final cooling was done by first quenching the glass to 500 °C to ensure that the heavier uranium did not precipitate out of the glass, followed by natural cooling to room temperature to prevent the introduction of thermal stresses in the glass structure. To check that the glass was free from phase separation the samples were inspected optically and with an electron microprobe. The samples were then cut and polished by SILO of Frienze to a planarity of λ/10, where λ is the sodium yellow line, and to a parallelism of 1/1000. A final polishing in water was carried out. The leaching was performed with a Soxhlet apparatus[17] in distilled, deionized water at 100

(35) Douglas, R. W.; El-Shamy, T. M. M. *J. Am. Ceram. Soc.* **1967**, *50*, 1.
(36) Boksay, Z.; Boquet, G.; Dobbs, S. *Phys. Chem. Glasses* **1968**, *9*, 69.
(37) Frischat, G. H. *Diffusion in Oxide Glasses*; Trans Tech Publications: Aedermannsdorf, Switzerland, 1975; p 89.
(38) Doremus, R. H. In *Treatise on Materials Science and Technology*; Tomozawa, M., Doremus, R. H., Eds.; Academic Press: New York, 1979; p 41.
(39) McVay, G. L.; Buckwater, C. Q. *Nucl. Technol.* **1982**, *51*, 123.
(40) Clark, D. E.; Hench, L. L. In *Scientific Basis for Nuclear Waste Management VI*; Brookins, D. C., Ed.; Elsevier Science: Amsterdam, 1983; p 113.
(41) Adams, P. B. *J. Non-Cryst. Solids* **1984**, *67*, 193.
(42) McGrail, B. P.; Pederson, L. R.; Peterson, D. A. *Phys. Chem. Glasses* **1985**, *26*, 35.
(43) Smets, B. M. J.; Lommen, T. P. A. *Phys. Chem. Glasses* **1983**, *24*, 35.
(44) Zachariasen, Z. W. *J. Am. Chem. Soc.* **1932**, *54*, 3841.
(45) Greaves, G. N.; Diakun, G. P.; Quinn, P. D.; Hart, M.; Siddons, D. P. *Nucl. Instrum. Methods Phys. Res.* **1983**, *208*, 335.
(46) McMaster, W. E.; Kerr Del Grande, N.; Mallett, J. H.; Hubbell, J. H. *Compilation of X-Ray Cross-sections*; TID 4500 UC-34 Physics.

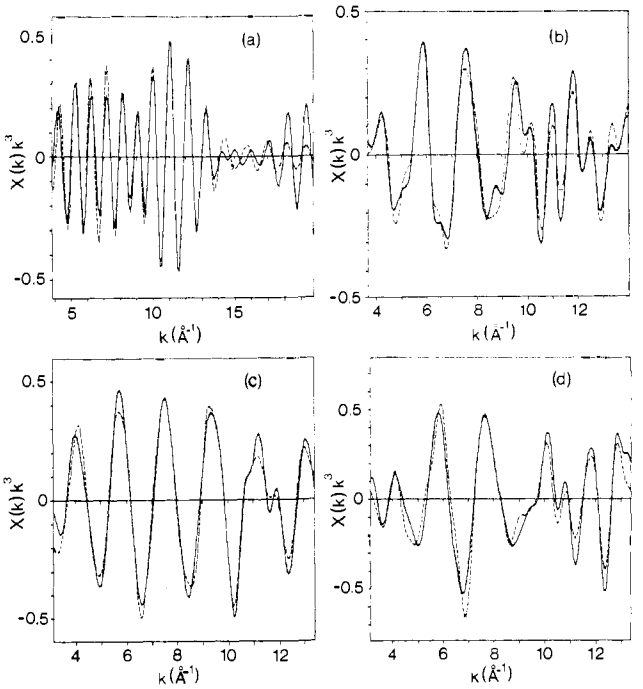

Figure 4. Fourier-filtered, k^3-weighted EXAFS data (solid lines) and least-squares fits (broken lines) for (a) U metal, (b) UO_3, (c) glass at 45° incidence (z = 0.5 mm), and (d) same glass after 90 min of leaching, at φ/φ_c = 2.0 (z = 1.4 μm).

°C. X-ray measurements were made immediately after leaching while the samples were still in their wet state. The leaching times used were 0, 15, 30, and 90 min. These times are similar to those already employed by other groups for the study of glass corrosion.[2] For each sample energy scans were made at φ/φ_c = 0.5 and φ/φ_c = 2.0, where φ_c = 1.8 mrad. The expected penetration depths are 40 Å and 1.4 μm, respectively (see Figure 1). In addition, the X-ray absorption spectrum of the glass was measured by tradiational fluorescence geometry, i.e., with the incident and the fluorescence beams at 45° to the sample surface to record the bulk structure. The penetration depth in this case was 0.5 mm. To calibrate the U L_{III} absorption threshold and to establish reliable phase shifts for the EXAFS in the glasses, the following reference compound spectra were recorded in transmission: uranium metal, uranyl fluoride fluoroammonium, U_3O_8, and UO_3. In order to have reference spectra representative of the main valence states of uranium, UO_2 was also measured.

3. Results

Results for the reference compounds are presented in Figures 3–5. Data were background subtracted by standard techniques and plotted as a function of k, where $k = (2m(E - E_0))^{1/2}/\hbar$, the photoelectron wave vector. Figure 3 shows the normalized raw data for the uranium metal weighted by k^3. This spectrum is typical of the quality of S/N for a transmission EXAFS spectrum. To carry out the least-squares analysis of the data, the higher frequencies originating from experimental noise and the lower frequencies originating from atomic EXAFS were filtered out in r space for $r > 5$ Å and $r < 1$ Å, respectively, leaving the spectrum shown in Figure 4a.

In Figure 4 are shown the Fourier-filtered EXAFS spectra for uranium metal, UO_3, the glass measured at φ = 45° (z = 0.5 mm), and the same glass after 90 min of leaching taken at φ/φ_c = 2.0 (z = 1.4 μm). The large differences in the fine structure in the models, for instance, demonstrate the sensitivity of X-ray absorption spectroscopy to local structure. The buildup of oscillations beyond 8 $Å^{-1}$ in the metal spectrum is a clear indication of structure in the uranium backscattering amplitude. This feature was absent in the uranyl spectrum where U–U correlations are weak but is present in the spectrum of UO_3 (Figure 4b). The oscillations below 8 $Å^{-1}$ are due to both U–O and U–U correlations. In the glasses, backscattering from Si shells is also expected in this spectral range. More to the point, in comparing parts c and d of Figure 4, it is clear substantial changes in structure can

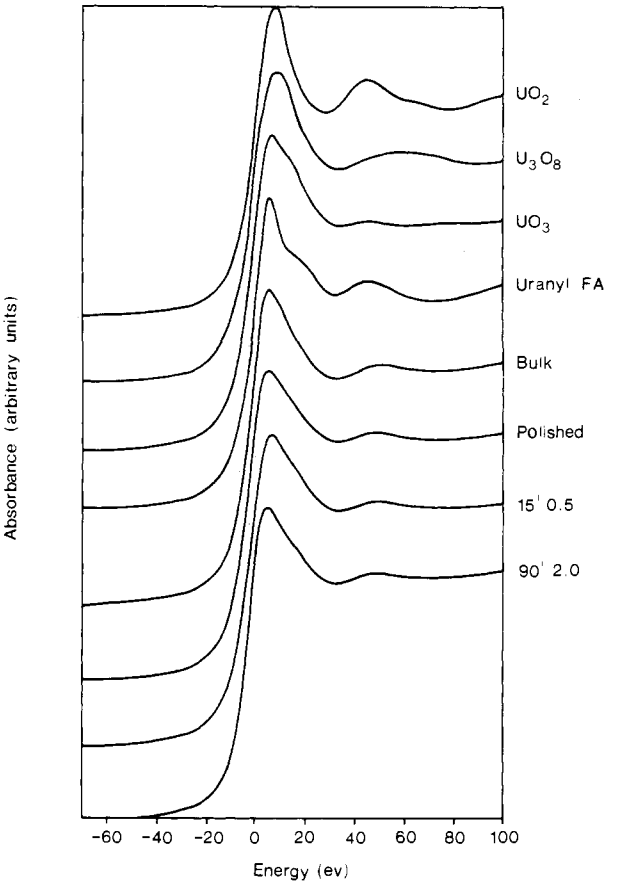

Figure 5. XANES spectra for a variety of oxides and glasses. The energy zero is taken as the turning point in the derivative spectrum of UO_2. The turning points of the higher valence oxides and glasses are shifted by ~1 eV with respect to UO_2. The differences in white line widths between the oxides and the glasses are evident in the position of the white line maximums; see also Table I.

Table I. White Line Half-Widths for the Reference Oxides Compared to Glasses at the U L_{III} Edge[a]

sample	white line widths	
	$E_{max} - E_{inf}$, eV	hwhm,[21] eV
UO_2	8.5	6.6
U_3O_8	9.1	7.1
UO_3	6.1	
UO_2F_2	4.7	5.6
bulk glass	6.0	6.2
polished 0.5	6.1	
glass C 0.5	6.4	
glass F 2.0	6.7	

[a] Widths measured by Petiau et al.[21] are included for comparison.

be recorded by employing different angles of incidence. In particular, the results of corrosion can readily be detected.

The XANES spectra for the various oxides are compared to the glass spectra in Figure 5. The white line width is taken from the difference in energy between the maximum in the absorption and the point of inflection in the absorption jump, $E_{max} - E_{inf}$. We observe a narrowing of the white line width by almost a factor 2 between UO_2 and the uranyl compound. The glass spectra have white line widths intermediate between these limits, as shown in Table I. Note in particular that leaching results in a broadening of the white line width. On the basis that the white line provides a map of empty states to which a photoelectron may make a transition, Petiau et al. proposed that the broader white line widths of UO_2 and U_3O_8 result from hybridization of the uranium 5f states with the 6d and 7s states and greater overlap with the oxygen 2p states in these more three-dimensional structures.[21] This is minimal in the layered uranyl compound where the uranium environment is quasi-octahedral. The widths of the white lines

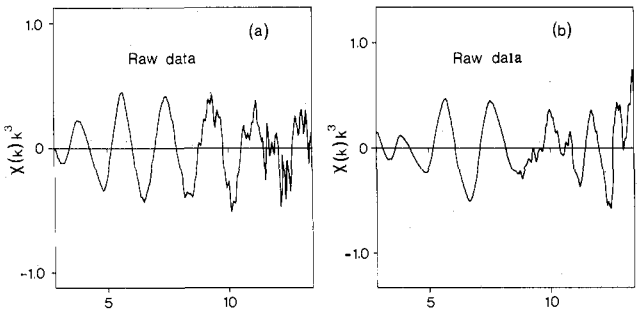

Figure 6. Background-subtracted, k^3-weighted raw EXAFS data for glasses taken at (a) 45° incidence, hence showing the bulk signal, and (b) $\varphi/\varphi_c = 2.0$, leaching time 90 min, showing the near-surface signal. The corresponding Fourier-filtered spectra are shown in Figure 4c and d.

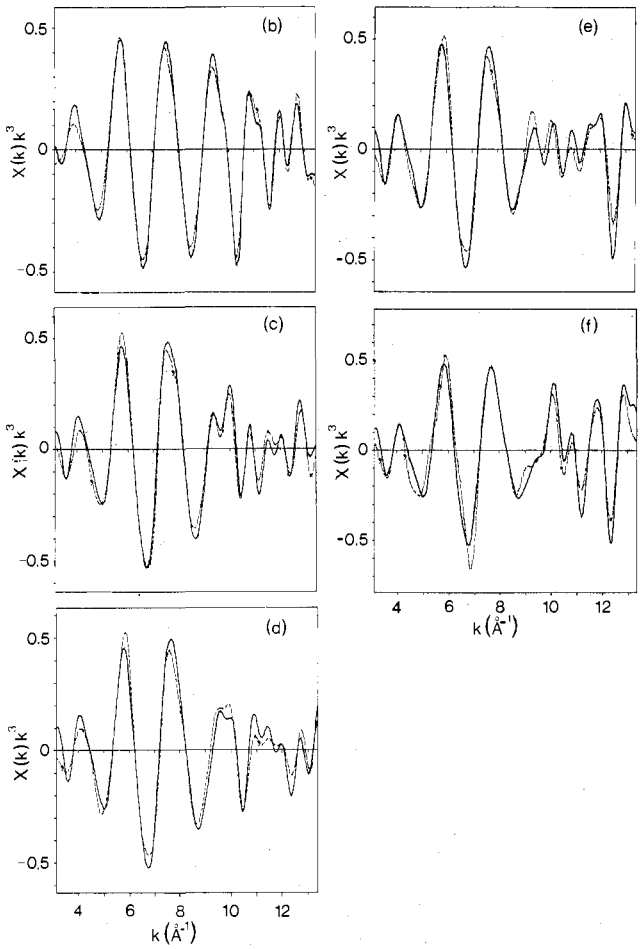

Figure 7. Fourier-filtered, k^3-weighted EXAFS spectra (solid lines) and least-squares fits (broken lines) for glasses taken at $\varphi/\varphi_c = 2.0$, corresponding to a penetration depth of ~ 1.4 μm, for the following leaching times: b, 0 min; c, 15 min; d 15 min and 8 h drying under vacuum; e, 30 min; f, 90 min.

in the glasses point to a slightly different structure. We will see later in analyzing the EXAFS spectra that leaching results in increased agglomeration of uranyl units, causing a change in hybridization, thus accounting qualitatively for the change in white line width.

In Figure 6 are shown the fluorescence EXAFS raw data for glasses taken at (a) 45° incidence showing the signal form the bulk structure and (b) $\varphi/\varphi_c = 2.0$, leaching time 90 min, showing the signal from the near surface structure. The corresponding Fourier-filtered spectra are shown in Figure 4c and d. While the S/N ratio is not quite as high as for the model compounds (see Figure 3), we will show that Fourier-filtered data out to ~ 13 Å^{-1} are adequate for detailed least-square analysis of the various pair correlation functions. In Figures 7 and 8 are shown the EXAFS

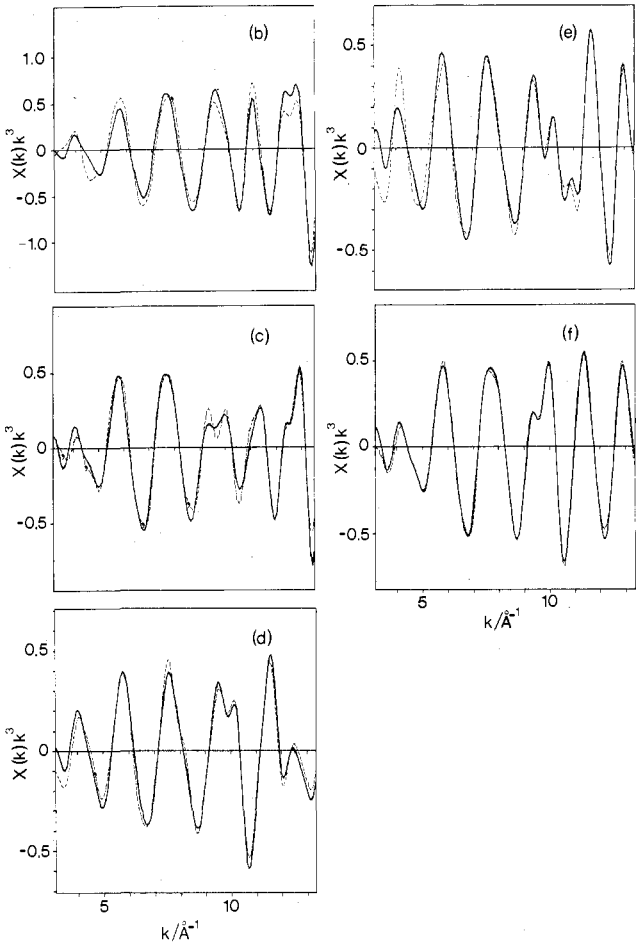

Figure 8. Fourier-filtered, k^3-weighted EXAFS spectra (solid lines) and least-squares (broken lines) for glasses taken at $\varphi/\varphi_c = 0.5$, corresponding to a penetration depth of ~ 40 Å, for the following leaching times: b, 0 min; c, 15 min; d, 15 min and 8 h drying under vacuum; e, 30 min; f, 90 min.

spectra taken at $\varphi/\varphi_c = 2.0$ ($z = 1.4$ μm) and $\varphi/\varphi_c = 0.5$ ($z = 40$ Å), respectively, for the leaching times given above. Differences can clearly be seen between the surface spectra as corrosion advances. Comparing pairs of spectra with the same leaching history taken above and below the critical angle reveals significant differences in the glass surface structure as a function of depth.

4. Data Analysis

In Figures 4, 7, and 8 the dotted lines indicate the fits to the experimental data obtained with the Daresbury EXAFS analysis program EXCURVE,[47] based on the curved wave theory of Lee and Pendry.[48] Taking the model compound spectra first, these were fitted by using as starting values crystallographic data. The phase shifts were calculated by using Herman–Skilman wave functions with the appropriate crystal structure by the Daresbury MUFPOT program.[49] They were then refined with a linear function of the photoelectron wave vector as a correction. The central atom and backscattering phase shifts were obtained for uranium by using the uranium metal spectrum and the oxygen backscattering phase shifts by using the uranyl compound. During the refinement, modest changes in the interatomic distances and the Debye–Waller factors were allowed to optimize the fit; however, the coordination numbers were held at the crystallographic values. The results with

(47) Gurman, S. J.; Ross, I.; Binsted, N. *J. Phys. C* **1984**, *17*, 143.
(48) Lee, P. A.; Pendry, J. B. *Phys. Rev. B* **1975**, *11*, 2795.
(49) Pantos, E.; Firth, G. D. *Springer Ser. Chem. Phys.* **1984**, *27*, 110.
(50) Binsted, N.; Greaves, G. N.; Henderson, C. M. B. *Contrib. Mineral. Petrol.* **1985**, *89*, 103.
(51) Greaves, G. N.; Gurman, S. J.; Gladden, L.; Spence, C.; Cox, P.; Sales, B. C.; Boatner, L. A.; Jenkins, R. N. *Philos. Mag.* **1988**, *B58*, 271.

Table II. Structural Parameters Obtained by EXAFS for the Uranium Reference Compounds following Refinement of the Atomic Phase Shifts[a]

	EXAFS					crystallogr	
sample	shell	atom	N	r, Å	$2\sigma^2$, Å^2	N	r, Å
U metal	1	U	2	2.76	0.013	2	2.754
	2	U	2	3.02	0.024	2	2.848
	3	U	4	3.26	0.015	4	3.258
	4	U	4	3.35	0.017	4	3.341
UO_2F_2	1	O	2	1.89	0.005	2	1.91
	2	F	6	2.47	0.005	6	2.50
UO_3	1	O	1	1.82	0.009	1	1.804
	2	O	1	1.91	0.007	1	1.846
	3	O	1	2.19	0.007	1	2.195
	4	O	1	2.25	0.014	1	2.220
	5	O	2	2.34	0.007	2	2.379
	6	O	1	2.51	0.018	1	2.557
	7	U	1	3.64	0.025	1	3.690
	8	U	1	3.96	0.022	1	3.985
	9	U	1	4.08	0.025	1	4.031
	10	U	1	4.20	0.011	1	4.176

[a] These are compared to the crystallographic data for U[53], UO_2F_2,[32] and UO_3.[52]

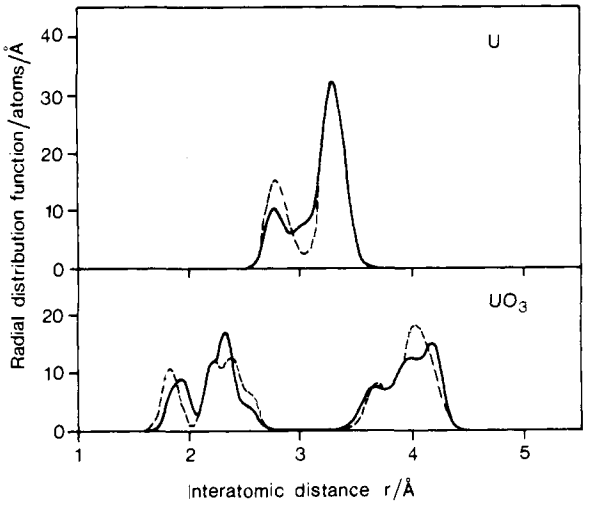

Figure 9. Partial radial distribution functions as determined from EXAFS (solid line) compared to crystallography (dashed line) for U[53] and UO_3.[52] These are Gaussian-broadened histograms of the fits presented in Table II. See text for details.

the refined phase shifts are given in Table II where they are compared to the starting crystallographic data. The phase shifts were then used to fit UO_3. The structure derived from EXAFS for UO_3 is also included in Table II and compared with the crystallographically determined structure.[52] With the appropriate phase shift modifications, the interatomic distances found from EXAFS generally agree with the crystallographic distances to 0.03 Å or better—the typical precision expected from the curved wave theory.[48]

Compared to a table of values, the overall accuracy of multiple-shell EXAFS analysis can more easily be judged from the partial radial distribution functions (prdfs) for U and UO_3 shown in Figure 9. These were constructed from the parameters obtained in the experimental fits and catalogued in Table II. Each atom–atom correlation is represented by an amplitude, given by the coordination number, N, a mean distance, given by the shell radius, r, and broadened by the Debye–Waller factor, σ^2. A real-space representation of this form is preferable to the customary Fourier transform of the EXAFS since it does not suffer from truncation errors due to the finite k range of EXAFS, it does not have to be corrected for the presence of phase shifts, possibly masking fine details, and it does not suffer from distortions of the plain

(52) Siegel, S.; Hoekstra, H. R.; Sherry, E. *Acta Crystallogr.* **1966**, *20*, 292.

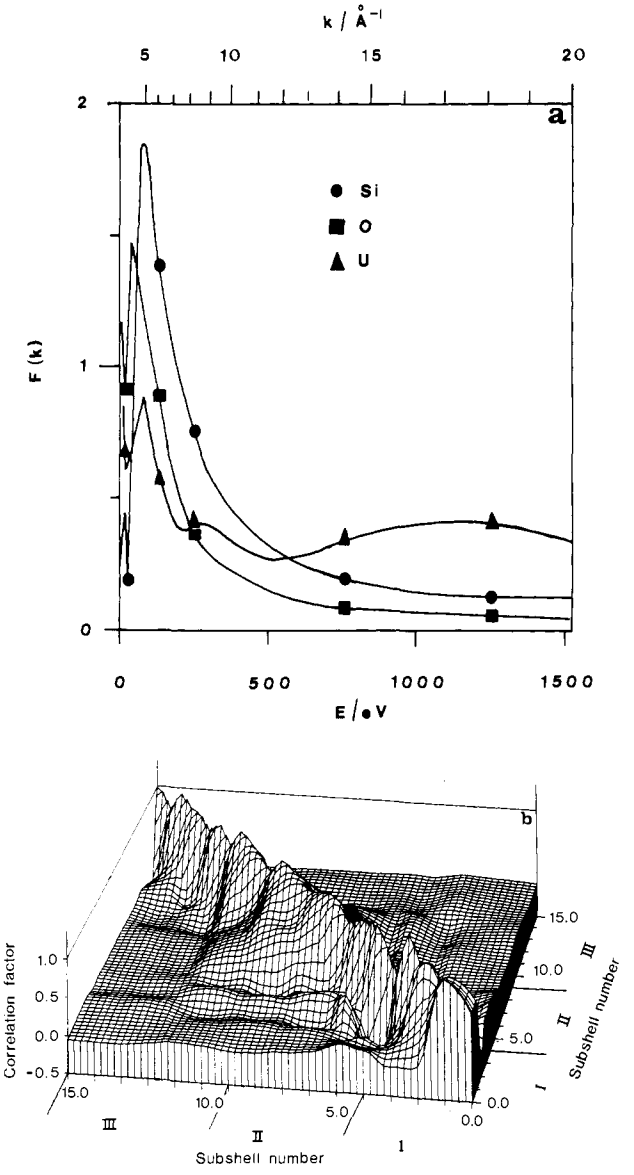

Figure 10. (a) Silicon, oxygen, and uranium backscattering amplitudes as calculated by MUFPOT. (b) Plot of the correlation matrix obtained for interatomic distances for a typical glass spectrum (φ/φ_c = 2.0, 90 min; Figure 7f). This shows the subshell grouping of oxygen, silicon, and uranium distances.

wave approximation inherent in making the Fourier transform. The direct comparison with crystallography that can be made in Figure 9 using Gaussian-broadened histograms gives a measure of the structural content present in the spherically averaged EXAFS signal. Note, for instance, how the intralayer and interlayer distances are resolved in the metal structure, and how the components of the oxygen and uranium ligands are well-reproduced for UO_3.

Both U and UO_3 have distorted crystalline structures and their EXAFS spectra carry about the same information content as the glancing-angle spectra of the borosilicate glasses. Figures 11 and 12 show the prdfs for the glasses as a function of leaching and angle of incidence. These Gaussian-broadened histograms were constructed, as described above, by using the shell radii, coordination numbers, and Debye–Waller factors associated with the EXAFS fits shown by dotted curves in Figures 7 and 8. It should be emphasized that where the structural disorder and the atom type of individual shells in crystalline models like U and UO_3 are already known from diffraction measurements, the equivalent information is of course not available for the glasses. Indeed, despite element specificity, EXAFS of glassy materials is structurally underdetermining and analysis is necessarily model de-

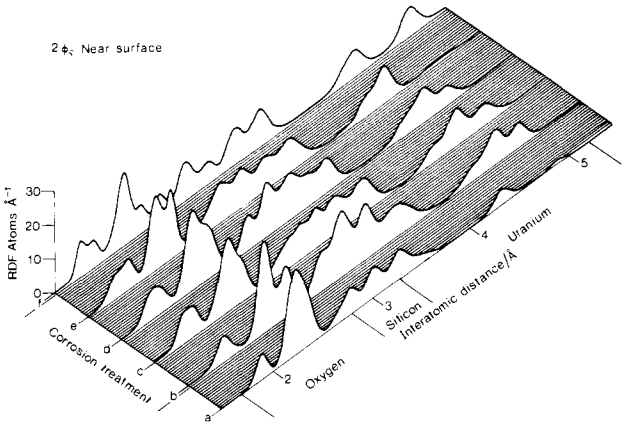

Figure 11. Partial radial distribution functions as determined from the EXAFS fits shown in Figure 7 for glasses taken at $\varphi/\varphi_c = 2.0$, as a function of corrosion treatment. They are presented in the following order: (a) bulk structure (measured at 45° incidence); (b) as received polished glass; (c) after 15 min of leaching; (d) after 15 min of leaching and subsequent drying for eight hours under vacuum; (e) after 30 min of leaching; (e) after 90 min of leaching.

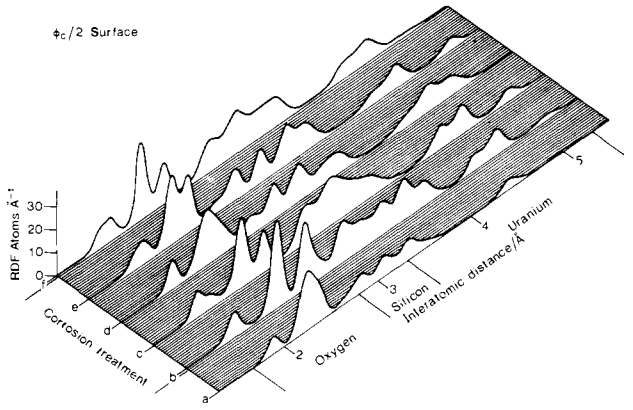

Figure 12. Partial radial distribution functions as determined from the EXAFS fits shown in Figure 8 for glasses taken at $\varphi/\varphi_c = 0.5$, as a function of corrosion treatment. They are presented in the following order: (a) bulk structure (measured at 45° incidence); (b) as received polished glass; (c) after 15 min of leaching; (d) after 15 min of leaching and subsequent drying for 8 h under vacuum; (e) after 30 min of leaching; (e) after 90 min of leaching.

pendent, except in the simplest of single-shell covalent systems. In analyzing the EXAFS spectra of the glasses shown in Figures 7 and 8 it was found necessary to consider several shells of atoms each divided into subshells to elicit the fine structural detail. This approach of multiple-shell analysis has been used with success in earlier studies of modifying cations in oxide glasses.[50,51] Indeed, in the present study the structures of U and UO_3 have been analyzed in this way (Table II and Figure 9). However, for the glasses, where the chemical as well as the structural architecture is unknown, care has to be taken in dealing with a protracted list of potentially variable parameters. Some constraints are essential if the modeled structures are to be physically meaningful.

In the first place, the maximum number of subshells is naturally governed by the band pass, Δk, of the EXAFS experiment. If Δr is the average separation of subshells, this is related to Δk, for a backscattering geometry, by

$$2\Delta r \Delta k \sim 2\pi$$

Taking $\Delta k \sim 10$ Å^{-1} (see Figures 7 and 8), the average separation of subshells $\Delta r \sim 0.3$ Å. For a real-space window extending to 5 Å, the largest number of subshells cannot exceed 15.

The second constraint concerns the intrinsic broadening of subshells. As each subshell relates more or less to discrete correlations between atom pairs, these should be free from the static disorder otherwise agglomerated through averaging whole coordination spheres. Accordingly, in this analysis subshells were only broadened by the *thermal* Debye–Waller factor obtained from the model compounds for individual nearest neighbor and next nearest neighbor shells (Table II). In UO_2F_2 the thermal FWHM for U–O corelations is ~0.1 Å, and as this is less than Δr, any static disorder on the scale 0.1–0.3 Å should, in principle, be resolvable. The fitting procedure we adopted to achieve this was to fix the Debye–Waller factor and allow subshell radii and occupancies to float. In this way, if the coordination sphere is free from static disorder, subshell radii will approach closer than 0.3 Å and coalesce within the thermal spread; otherwise the overall shell width will broaden to encompass local distortion and site variation. In some cases subshell structure will emerge, which is what we observe for uranium in the present borosilicate glasses. Subshell occupancies will add or substract to match the contribution each makes to the total coordination number of the shell. The practicalities of multiple-shell fitting have already been demonstrated in studying the oxygen shells of various metal sites in minerals and oxide glasses.[50,51]

We will show later that it is changes in the makeup of the oxygen shell that are chiefly responsible for the dramatic changes in U L_{III} EXAFS as corrosion advances. However, there are also significant contributions to the EXAFS that derive from next neighbor cation shells. Because of the considerable differences in backscattering afforded by oxygen, silicon, and uranium, some chemical constraints are necessary in associating atom types with each of the major subshell groupings. These in turn can affect the total coordination numbers that are derived for each atom type and this information can then be used to improve the uniqueness of the model structure. The backscattering amplitudes for oxygen, silicon, and uranium, as calculated by MUFPOT are presented in Figure 10a. Clearly, beyond 8 Å^{-1} uranium atoms are stronger backscatters compared to oxygen atoms. The onset of U–U correlations in UO_3 can be clearly seen in the normalized fine structure shown in Figure 4b.

Qualitatively the same behavior appears to occur in the glass spectra shown below (Figure 4c and d). Accordingly, we first attempted to model the local structure of U in the glasses by U–O correlations extending from 1.6 to 3.0 Å and U–U correlations from 3 to 5 Å. This rough criterion, however, led to unnaturally high oxygen coordination numbers (i.e., greater than 9) and was abandoned in favor of including U–Si correlations at intermediate distances. Figure 10a indicates that out to 12 Å^{-1} silicon is a comparable backscatter to uranium; thereafter uranium dominates. U–Si correlations were therefore chosen at distances from 2.7 to 3.3 Å. Given the Si–O bond length of 1.6 Å and an equatorial U–O bond length of 2.3 Å, then such U–Si separations would occur for the reasonable bond angles at nonbridging oxygens of 90 to 120°. Introducing silicons into the model structure in this way meant that while individual subshell radii were only modestly affected overall, meaningful oxygen coordination numbers were restored (i.e., less than 9)—adding support to the identification of silicon as a next nearest neighbor. We will show later (5.4.) that, quite apart from the distinguishing character of the different backscattering factors for neighboring atoms, there is also considerable internal consistency in the distribution of oxygens and the U–U correlations analyzed for each glass spectrum.

In summary, the near-surface and surface EXAFS plotted in Figures 7 and 8 have been analyzed by multiple-shell least-squares fitting for environments comprising oxygen, silicon, and uranium neighbors. The natural constraints of band pass and thermal broadening and the ramifications of different backscattering factors substantially improve the uniqueness of the fits shown in Figures 7 and 8. This can be most readily judged by examining correlations between the r and N parameters of the different subshells and the fit index f_i. The correlation matrix of the fit index for r values if shown in Figure 10b as an example for one of the spectra (shown in Figure 7f). The fit index is given by

$$f_i = \sum \frac{((\chi_{\text{theory}} - \chi_{\text{expl}})k^3)^2}{n} \times 100$$

A positive number means that the fit can be improved by moving either r value of the subshell pair in the same sense. The converse

Table III. U-O Bond Lengths for a Selection of Oxides, Silicates, Uranates, and Uranyl Hydrates[a]

chemical formula	oxygen bond lengths, Å						ref
UO_2					(8)2.37		53
$Na_2UO_2SiO_4$			(4)2.03		(2)2.29		58
$USiO_4$					(4)2.32	(4)2.51	57
UO_3	(1)1.80	(1)1.85	(1)2.20	(1)2.22	(2)2.38	(1)2.56	52
Na_2UO_4		(2)1.89	(2)2.18	(2)2.21			55
$Na_2U_2O_7$		(2)1.92			(6)2.31		56
$CaUO_4$		(2)1.96			(6)2.30		32
$UO_2(OH)_2$		(2)1.79			(4)2.46	(2)2.51	59
$K(UO_2)_2(Si_2O_5)_3(H_2O)_4$		(2)1.81	(2)2.22	(1)2.28		(2)2.58	60
$MgO(UO_3)_2(SiO_2)_2(H_2O)_7$	(1)1.66	(1)1.75		(2)2.23	(1)2.32	(2)2.55	61

[a] These demonstrate the variety of configurations possible in two- and three-dimensional structures and are used as a guide to interpret the corrosion processes taking place in the surface of the glass. The coordination numbers of the subshells are shown in parentheses. See text for details.

applies for a negative number. The subshell groupings, I, II, and III in Figure 10b correspond to oxygen, silicon, and uranium character. While some mixing of subshells of different atom type was permitted, the chemical character of each subshell grouping remained predominantly pure. The obvious diagonal character of the correlation matrix shown in Figure 10b removes much of the amgituity in the identification of subshell structure. The absence of any major off-diagonal features means, for instance, there is little correlation between the nearest neighbor oxygen shells and more distant cation shells. Moreover, we can see in Figure 10b that there are several distinct features within each of the major subshell groupings. The overall diagonal profile of the correlation matrix in fact closely matches the prdf shown in Figure 11f, indicating that these finer details are indeed significant. An almost identical picture emerges for the fit index matrix of N values. The characteristics of Figure 10 are also displayed by all the glass spectra.

The uranium environments that are plotted in Figures 11 and 12 demonstrate a rich and varied structure. The corrosion-driven changes at and near the surface are considered in the next section.

5. Discussion

The results of the analysis of the uranium L_{III} glancing-angle EXAFS measurements presented in Figures 11 and 12 are arranged in the following order. The prdf measured at 45° to the sample surface (a) is compared first to the untreated polished surface measured at glancing angles (b). The surface leached for 15 min is presented next (c). The third prdf corresponds to a sample also leached for 15 min but then dried under vacuum for 8 h (d). The final two distributions refer to surfaces of samples leached for 30 (e) and 90 min (f), respectively. This arrangement of prdfs is common to both figures. Distributions a–c reveal information about the polishing treatment, c and d about the effects of drying, and c, e, and f about the process of leaching. As outlined earlier, the different angles of incidence employed confer different X-ray penetration depths. The near-surface region ($z = 1.4$ μm) is probed in Figure 11 where the angle of incidence sas $2\varphi_c$. The surface region ($z \simeq 40$ Å) is highlighted in Figure 12 by using an angle of incidence of $\varphi_c/2$. With incident radiation presented at 45° to the sample surface the penetration depth increases to ~0.5 mm, so prdf a in the two figures relates to the glass structure in the bulk that was unaffected by the degree of corrosion treatment explored in these experiments. Finally, the ranges of interatomic distances employed for oxygen (1.6 → 2.6 Å), silicon (2.7 → 3.3 Å), and uranium (3.3 × 5.2 Å) neighbors outlined in the previous section are also indicated in Figures 11 and 12.

5.1. Uranium Environment in the Bulk Glass. The most obvious feature of the uranium atomic distributions collated in Figures 11 and 12 is the split shell of nearest neighbor oxygens. There is often structure within these oxygen subshells that will be considered later. In the 45° bulk structure (a), however, there are just two distinct oxygen distances: a subsiduary subshell at 1.9 (5) Å with the majority of oxygen neighbors centered at 2.2 (9) Å. The total oxygen coordination number is 7 (4). Knapp et al.[28] and Petiau et al.,[21,34] who have used transmission EXAFS to measure the uranium environment in silicate and borosilicate glasses, report a similar splitting. Comparison with crystalline uranyl compounds suggests uranium in these oxide glasses has a similar distorted octahedral oxygen coordination sphere. As we have seen, uranyl bonding is characterized by two short axial oxygens close to 1.8 Å and four or more equatorial oxygens generally spaced between 2.2 and 2.5 Å. Uranyl bonding promotes layered structures.[32] The axial and equatorial bond lengths are influenced by the total coordination number, by the types of cation neighboring uranium, and by the degree of interlayer bonding (see Table III). The level of uranium used in our fluorescence EXAFS measurements is 0.2 atom %, and this demonstrates that the uranyl-type configuration found at higher concentrations[28,34] persists at levels of dilution representative of those required for nuclear waste disposal, given preparation under oxidizing conditions.

The EXAFS-derived prdfs for uranium metal, UO_3, and uranyl fluoride fluorammonium are contrasted to the prdf for the bulk glass structure in Figure 13. Compared to the various uranium environments in the model compounds we can see the oxygen splitting in the glass resembles the uranyl-like units found in UO_3[52] and the well-ordered uranyl fluoride fluoroammonium[32] but bears little relation to UO_2[53] where uranium occupies a regular eightfold site. The oxides of uranium display a multiplicity of phases;[54] however, these broadly divide into fluorite or uranyl-like structures. The two basic geometries can be distinguished in the following way: fluorite structures are three dimensional and cubic, while uranyl structures adopt orthorhombic, quasi two-dimensional geometries—the equatorial oxygens cross-linking to form distorted sheets.[32,54] Both types of structure offer enormous versatility for accommodating nonstoichiometry, the fluorites through varying numbers of interstitial oxygens and the uranyls through more or less equatorial oxygens. With such degrees of flexibility there is no a priori structural reason for predicting a preference for either type of environment for the uranium dissolved in an oxide glass. However, there is a tendency in crystalline oxides toward the lower density uranyl structures as the oxidation state of uranium increases from IV to VI. As we have seen, the predominant oxidation state in the glass if U^{6+}, judging from the position of the L_{III} absorption edge (see Figure 5). The width of the white line also points to a hybridization more typical of the uranyl group (Table I). Indeed this is slightly narrower in the glass than in UO_3 but not as narrow as in uranyl fluoride fluorammonium, suggesting that the degree of order for the oxygen coordination sphere in the glass is intermediate between these two structures. The atomic distributions included in Figure 13 provide more compelling evidence. The nearest neighbor configuration in the glass is quite distinct from that in UO_2 with its single shell of oxygens. Furthermore, the sharpness of the primary and secondary oxygen peaks of the glass is indeed intermediate between uranyl fluoride fluorammonium with its regular hexagonal layer structure and the distorted orthorhombic structure of UO_3.

(53) Wyckoff, R. N. G. *Crystal Structures*; Wiley: New York, 1964; Vol. 1, p 243.
(54) Weigel, F. In *Chemistry of the Actinide Elements*; Katz, J. J., Seaborg, G. T., Morss, L. R., Eds.; Chapman and Hall: London, 1986; Vol. 1, p 169.

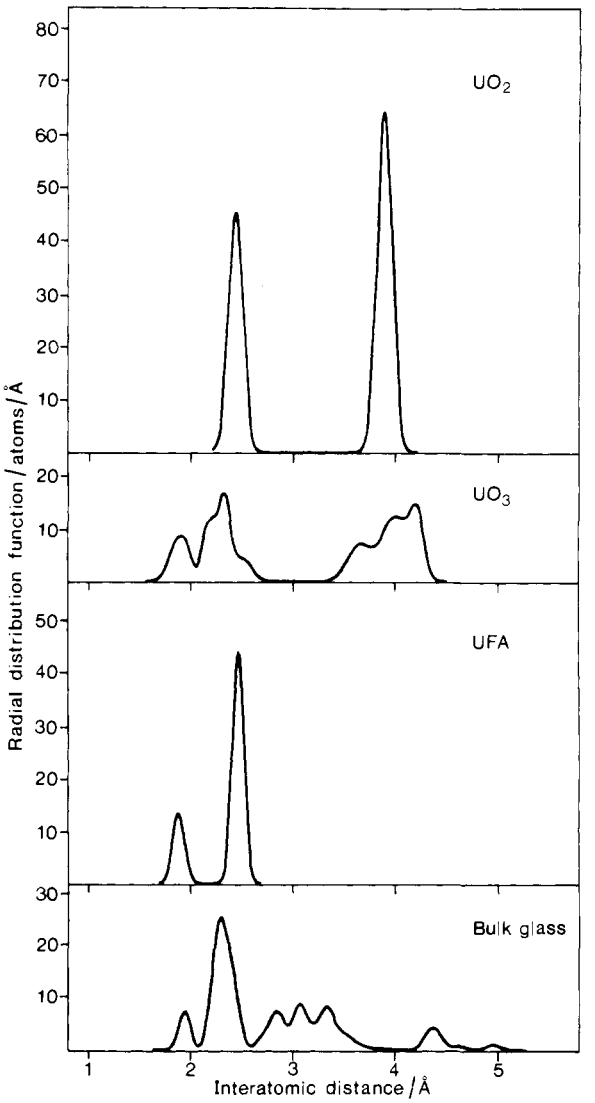

Figure 13. Partial radial distribution functions as determined from EXAFS for (a) UO_2, (b) UO_3, (c) uranyl fluoride fluoroammonium, and (d) bulk structure of the glass, showing that in the bulk glass the U–O coordination lies between that for UO_3 and that for the uranyl compound.

In addition to nearest neighbor oxygens, analysis of the EXAFS from the bulk glass reveals some weaker correlations with surrounding cations. Interestingly, where UO_3 (and UO_2) exhibits no intermediate shells between 2.4 and 4 Å, the glass structure is different. There is clearly a shell close to 2.9 Å, which we ascribe to silicon neighbors, with another around 3.1 Å. Between 3.3 and 4 Å correlations are better fitted by uraniums because the backscattering from silicon is insufficient to reproduce the increased amplitude of the fine structure beyond 10 $Å^{-1}$ (Figures 7 and 8). Finally, as in the uranium oxides, there are shells around twice the U–O distance that almost certainly can be ascribed to uranium atoms. Qualitatively the same situation has been reported for higher concentrations of uranium in oxide glasses.[28] Moreover, evidence for larger numbers of U–U correlations was found for increased concentrations. In the present case with the dilution of uranium at the 0.2 atom % level, if the metal were evenly distributed throughout the glass the average U–U separation would be between 15 and 20 Å. Accordingly, with spacings detected in the 3.3–5-Å range, some clustering must be taking place in the bulk glass. A striking feature of Figures 11 and 12 is that clustering is exaggerated both at the surface and in the near-surface region of the glass by corrosion treatment compared to the bulk. The microscopic aggregation of uranyl-like groups in oxide glasses can be understood by reference to the modified random network model (MRN)[20]—particularly if uranium acts as a modifying cation in the glass structure. The topological aspect

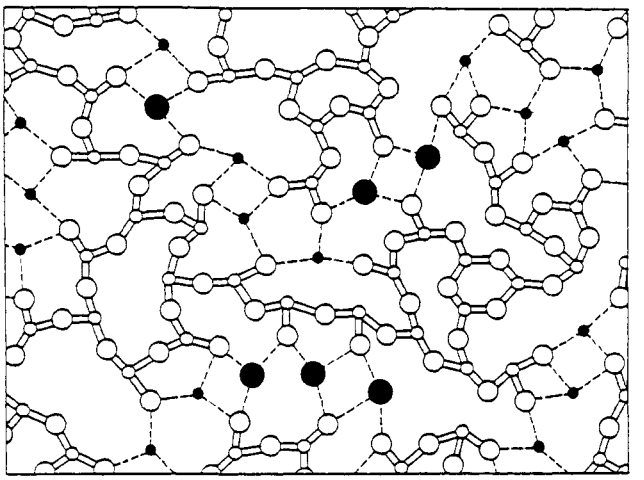

Figure 14. Modified random network (MRN) model for glass structure.[20] Glass former cations are small open circles, oxygen atoms are the large open circles, glass modifier cations are small filled circles, while the uranium atoms, which are also modifiers, are the large filled circles. There are two basic interconnected subnetworks. The uranium is prsent as a modifier cation within the modifier network, accounting for its higher mobility and clustering. Note that this drawing does not attempt to reflect the real ratio of Na to U, but only to illustrate the possible uranium sites.

of assembling regular modifier units juxtaposed with regular network units in an otherwise random structure is shown schematically in two dimensions in Figure 14. The modifier units, which comprise the smaller fraction, congregate into islands or filaments within the covalently bonded random network. For the borosilicate glass in question, the network or glass-former region would consist of rings and chains of Si–O and B–O bonds with modified regions made up chiefly of NaO_x unit. As far as uranium is concerned, it is not immediately obvious in the context of a MRN whether this cation would enter the modifier or network component. With its varied oxide configurations, uranium, like iron or titanium for instance, could be regarded as an intermediate glass former. However in the present situation, if the uranium occupied network sites, the average U–U separation would not be less than 15 Å, making spacings as short as 4 Å unlikely (Figures 11 and 12). On the other hand, with uranium residing in the modified regions it would occupy ~2% of the available sites resulting in an average separation of ~9 Å, which is more closely in line with the clustering that is observed.

More direct evidence that uranium occupies modifier positions in the borosilicate glass comes from the uranyl-like configuration. The oxygen local structure of a selection of uranates and uranium silicates are given in Table III. In the uranates Na_2UO_4[55] and $Na_2U_2O_7$[56] the short and long bonds are at 1.9 and 2.2 or 2.3 Å, which are very similar to the two oxygen subshell distances in the bulk glass. The same is true of $CaUO_4$.[32] It is interesting to note that uranyl groups in these uranates, while they form regular tetragonal or hexagonal layers,[32] also exhibit some interlayer interaction, which results in the axial oxygen bonds being lengthened compared to the usual 1.8 Å value. Although hydrated uranyl silicates exhibit uranyl bonding, this is not the case in $USiO_4$[57] or in $Na_2UO_2SiO_4$.[58] In $USiO_4$ uranium sites are eightfold with four neighbors at 2.32 Å and four more at 2.51 Å. On the other hand, the uranium sites in $Na_2UO_2SiO_4$ are distorted octhaedra, but unlike the uranyl environment, the weighting is revesed with four shorter bonds at 2.03 Å and two longer bonds to 2.29. These are clearly not good models for the uranium environment found in the glass, which suggests uranium

(55) Kovba, L. M. *Radiokhimiya* **1971**, *13*, 309.
(56) Kovba, L. M.; Ippolitova, E. A.; Simanov, Yu P.; Spitsyn, V. I. *Dokl. Akad. Nauk SSSR* **1958**, *120*, 1042.
(57) Fuchs, L. H.; Gebert, E. *Am. Mineral.* **1958**, *43*, 243.
(58) Shashkin, D. P.; Lur'e, E. A.; Belov, N. V. *Kristallografiya* **1974**, *19*, 958.

is not part of the network structure. Rather, the close similarly between the lengths and weighting of the short and long oxygen bonds in the glass with those found in alkali uranates points to uranium occupying the modified regions of the glass structure as depicted in the MRN model (Figure 14). Note, however, that modifiers will generally be linked via nonbridging oxygens to the network, so a 2.9-Å U–Si distance is to be expected.

The principles we have introduced that govern the actanyl-like configuration of uranium in the glass structure will now be used to consider the corrosion processes taking place at or near the surface—in particular the effect of the incorporation of water.

5.2. Near-Surface Uranium Environment. The prdfs presented in Figure 11 relate to an X-ray penetration depth of between 1 and 2 μm. This is similar in size to the depletion layers reported from analytical measurements.[37] Not surprisingly, there are significant changes in the near-surface environment of uranium as a result of corrosion treatment. Notably the oxygen subshells at 1.9 and 2.3 Å develop structure, suggesting different types of uranyl-like units are being generated. Also the cation shells are more pronounced, indicating more extensive clustering close to the surface compared to the bulk.

As described at the outset sodium is known to leave the glass as leaching advances and is replaced by protonated water. We have argued uranium resides in the modified regions of the glass structure, and so with the departure of sodium and the ingress of water, the reconfiguring of the uranium environment is most easily explained by the formation of hydrated species. Substructure in the oxygen distributions can be seen clearest in the prdfs of specimens leached for 30 and 90 min (e and f, respectively). Compared to the bulk glass structure (a) there is now a shorter "axial" oxygen bond at 1.8 Å and a longer "equatorial" bond at 2.4 Å. This environment closely matches the uranium local structure in $UO_2(OH)_2$,[59] which has two short oxygens at 1.79 Å with six longer ones close to 2.5 Å (Table III). Hydrated oxides like $UO_2(OH)_2$ are in fact topologically equivalent to the alkali uranates forming infinite sheets from the equatorial oxygen bonds.[32] There are, however, two main distinctions. First, a reduction in interlayer bonding in $UO_2(OH)_2$ leaves the axial oxygens shorter than the alkali uranates. Second, the absence of the electronegatively strong alkali cations is responsible for the longer equatorial bond lengths in the hydrate. We will find further evidence for this assignemnt of the 1.8 and 2.4 Å peaks in the changes that take place at the surface as a result of drying (Figure 12, c and d). Among the prdfs in Figure 11 a further oxygen subshell can be distinguished around 2.6 Å. It is clearly present in the as-polished distribution (b). It disappears in the initial stages of leaching (c and d) but returns after prolonged treatment (f). In addition to $UO_2(OH)_2$, Table III lists details of the uranium configurations in the hydrated uranyl silicates weeksite[60] and sklodowskite.[61] In these minerals uranyl groups bond to SiO_4 units to form uranosilicate layers with the alkali or alkaline-earth cations occupying the interlayer regions. As in $UO_2(OH)_2$ the interlayer bonding is weak, leaving the axial oxygen bonds shorter than in the uranates. The equatorial oxygen bonds, on the other hand, tend to be split leaving several around 2.2 Å and the remainder at 2.6 Å rather as in UO_3 (Table III). The as-polished specimen conforms well to this three-peak distribution (Figure 11). It is well-known that polishing often strongly affects the submicron surface structure and it would appear that the process employed here has resulted in the formation of a hydrated layer at the surface. However, comparing prdf b and c, it is clear that leaching in water at 100 °C for 15 min results in the replacement of the three-peak structure with the simpler two-peak structure reminiscent of modifying uranyl-like groups in the bulk glass. This would indicate that the polished surface has been removed. Interestingly, drying the treated surface (prdf d) has little effect as judged over the top few microns. On the other hand, prolonged leaching for up to 90 min (prdfs d–f) results in the reappearance

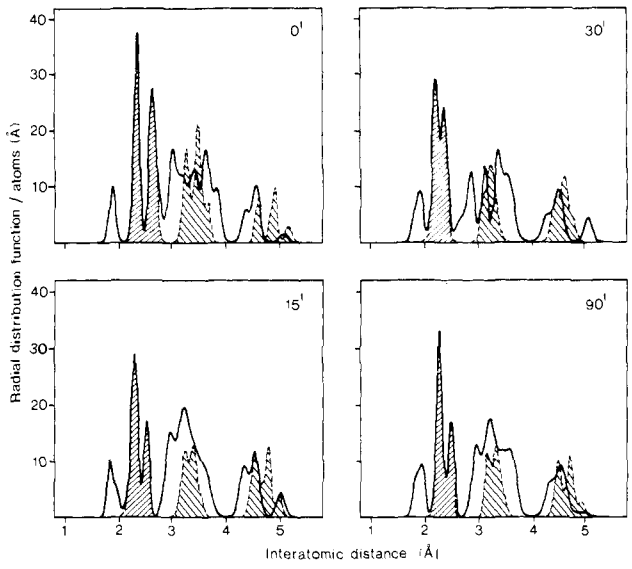

Figure 15. Prdfs obtained for surface spectra ($\varphi/\varphi_c = 0.5$) of glasses b, c, e, and f (solid lines) and the U–U correlations predicted from the equatorial oxygen distributions using the square-planar lattice model. See text for details.

of the 2.6-Å oxygen bond in the near-surface structure, suggesting the buildup of hydrated uranyl silicate like groups once more. As we have already noted, the 1.9- and 2.2-Å peaks are split, indicating the uranyl hydroxide type complexing is also present near the surface.

The following picture emerges from consideration of the prdfs in Figure 11. The dominant uranium species formed near the surface as a result of lapping and polishing appear to be hydrated uranyl silicates. These are removed by modest leaching to reveal a fresh surface similar to the bulk that we have likened to the local structure in sodium uranates. Continued leaching results initially in the formation of uranyl hydroxide type groups: this would be the natural outcome of ion exchange with water groups such as H_3O^+. These complexes convert finally to hydrated uranyl silicates, the end product of the corrosion treatment. This scenario is consistent with the generation of a gel layer at the surface of leached borosilicate glasses and the formation of a surface precipitate.[4,14,41] It establishes uranium, like sodium, as a modifying cation in the glass structure, as illustrated in Figure 13. Uranium is therefore expected to be mobile, which would explain the tendency for uranyl groups to cluster. It is worth noting, for instance, that polynuclear complexes of actinyl ions are readily formed in solution.[62]

In Figure 11 the shells around 3.4 and 4.4 Å, which have been assigned to uraniums in the bulk structure (prdf a), are certainly more heavily occupied near the surface (prdfs b–f). The locations of these two groups of U–U correlations correspond roughly to $2^{1/2}R$ and $2R$, where R is the average equatorial-like oxygen bond length in the glass. This relation betwee first and second nearest neighbors is reminiscent of square-planar complexing.[28] Indeed we will demonstrate later that the secondary oxygen distribution can be used to predict the uranium correlations in the prdf (Figure 15).

5.3. Uranium Environment at the Surface. As we have already emphasized, by measuring fluorescence EXAFS with the radiation incident below φ_c, the penetration of the X-rays is reduced, in principle, to a few tens of angstroms from eq 2. However surface sensitivity is affected by the flatness of the specimen or figure, and the quality of the surface finish, or roughness. While the figure of the polished flats used was of optical quality (overall figure $\ll \varphi_c$) and unlikely to be altered by the degree of corrosion treatment employed, the surface roughness visually deteriorated

(59) Taylor, J. C.; Hurst, H. J. *Acta Crystallogr. B* **1971**, *27*, 2018.
(60) Stohl, F. V.; Smith, D. K. *Am. Mineral.* **1981**, *66*, 610.
(61) Mokeeva, V. I. *Kristallografiya* **1964**, *9*, 277.
(62) Ahrland, S. In *Chemistry of the Actinide Elements*; Katz, J. J., Seaborg, G. T., Morss, L. R., Eds.; Chapman and Hall: London, 1986; Vol. 2, p 1480.

with extended leaching. However, for the roughness to impair the surface sensitivity of glancing-angle measurements, the aspect ratio of the etched regions (depth/diameter) must be less than the critical angle, i.e., $<1.8 \times 10^{-3}$ rad. Considerable surface sensitivity was achieved, as can be judged by comparing the $\varphi_c/2$ prdfs in Figure 12 with the equivalent $2\varphi_c$ prdfs from Figure 11, which indicates that surface roughness generated by corrosion was not a serious problem. While there are some general similarities between the near-surface and the surface structure, there are significant differences in detail—notably in the oxygen coordination sphere. Vestigates of the same corrosion process can be seen, but in a more rapid cycle.

The atomic distribution at the surface for the "as-polished" specimen (Figure 12b) is rather similar to the near-surface environment (Figure 11b). The same three-peak oxygen profile is resolved, indicative of hydrated uranyl silicate groups; the only significant difference is the increased weight of the 2.6-Å "equatorial" bond. Clearly the polished surface is reasonably homogeneous to a depth of a few microns. From prdfs b and c in Figure 11 it was concluded that the polished surface was removed by the initial 15-min leaching. In Figure 12 prdf c has the four-peak oxygen profile we have associated with a mixture of uranyl hydroxide like complexes and the alkaline uranate environment characteristic of the bulk. Evidently, at this early stage, corrosion of a new surface is already taking place. Turning now to the surface prdf of the dried specimen (Figure 12d), the oxygen distribution has the simple two-peak distribution of the uranate-like environment found in the bulk and also near the surface (Figure 11d). The comparison between the wet and dried surface prdfs (Figure 12c and d) is striking evidence that the extra uranyl configurations we have observed following leaching are indeed associated with water. It nicely demonstrates the surface sensitivity of glancing-angle EXAFS and the appropriateness of this geometry for the study of real surfaces.

The remaining prdfs in Figure 12 (e and f) suggest more extensive corrosion taking place at the surface than in the top few microns. In particular, the 2.6-Å peak we have associated with the hydrated uranyl silicate like group is well in evidence after 90 min of leaching. Indeed, there is less indication of uranyl hydroxide like complexes and the surface is beginning to resemble the as-polished specimen, reinforcing the cyclic character of the corrosion process outlined in the previous results.

5.4. Model for Uranyl Complexing. It has already been pointed out that U–U correlations occur predominantly in two broad subshells in the glass structure and that the location of these with respect to the second oxygen subshell at 2.3–2.6 Å suggests that the uranyl-like units complex into islands having square-planar geometry. Accordingly, it should be possible to predict the shape of the uranium distribution in the glass from the distribution of secondary oxygens. This is done in Figure 15 for the $\varphi_c/2$ prdfs. In each case the occupancies of the two uranium shells, normalized to the number of secondary oxygens, have been used to weight the $2^{1/2}R$ and $2R$ distributions derived from the shape of this oxygen subshell. Considering the simplicity of the model, the consistency between square-planar geometry and the analyzed oxygen and uranium distributions is surprisingly good for most of the prdfs. Note that the "unpredicted structure" falling between the oxygen and uranium components at 2.8–3.2 Å is in fact what we have previously attributed to U–Si corrleations. For an infinite two-dimensional simple square-planar lattice, there is one cation in each of the diagonal ($2^{1/2}R$) and edge ($2R$) sites for every near neighbor anion—and vice versa. However, for the uranium prfds analyzed here the occupancies of the two cation positions were fractional, indicating clusters of finite size. Now the number of secondary or "equatorial" oxygens measured in the bulk was 6.(3) and the average in the near-surface and surface regions was 6.(5). In an infinite square-planar latice, however, cations (and anions) occupy fourfold sites. The extra equatorial oxygens found in the uranium environment in the glass are consistent with a square-planar geometry if clusters are of finite size with a significant fraction of uraniums located at the peripheries bonding into the host glass structure. Indeed, the average size of the clusters is likely to be governed by this constraint.

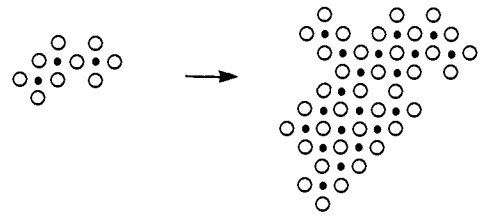

Figure 16. Clusters generated by using the experimentally determined coordination numbers for oxygen and uranium on the basis of a square-planar uranyl-type lattice to represent island formation in the bulk glass (left) and at the surface after 30 min of leaching (right). Uranium atoms are shown in black.

Eden's method for random cluster formation[63] has been used to model the size and shape of uranyl-like complexes consistent with the prdf coordination numbers. Starting with a simple uranyl unit, neighboring units were added successively on a random basis until the average environment of each uranium atom in the cluster approached the fractional occupancies of the $2^{1/2}R$ and $2R$ shells. Two cluster geometries obtained in this way are illustrated in Figure 16. This contrasts the bulk glass structure with the near-surface structure after leaching. The analyzed uranium coordination increases by approximately ×4, and despite a 10–20% uncertainty in matching the cluster geometry to this, the increase in cluster size is significant and striking. Figure 16 demonstrates pictorially the start and end of the leaching process.

Returning to the MRN model (Figure 14), we expect the small uranyl-like clusters in the bulk to be coordinated via sodiums into the modified regions of the glass structure. These in turn are tethered to the borosilicate network by the "so-called" nonbridging oxygens. The MRN predicts that the modified regions become the channels for ionic diffusion.[20] Accordingly, as leaching advances these are the zones in the glass structure where ion exchange will occur—a process tending to draw sodium and indeed uranium to the glass/liquid interface. In particular, as uranium builds up near the surface, complexing is likely to occur. This is the transition depicted in Figure 16. Finally, because uranyl-like complexes are bonded through nonbridging oxygens to the network, the removal of sodium at the surface and accompanying the dissolution of the borosilicate matrix will provide the ingredients for the recondensation of hydrated uranyl silicate complexes. It is this reprecipitation process which appears to inhibit the further dissolution of uranium. These predictions from the MRN model endorse the observed changes in the uranium environment from the bulk to the near-surface (Figure 11) and surface regions (Figure 12) and provide a viable description of the corrosion process occuring in uranium-containing borosilicate glass.

6. Conclusions

In this paper we have demonstrated how glancing-angle fluorescence EXAFS can be applied to study a major problem in corrosion. The uranium L_{III} EXAFS in a nuclear waste glass has been probed as a function of depth and as a function of leaching in water at 100 °C. In the bulk glass we find, as others have done but in this case in low concentrations, that the uranium adopts a uranyl-like configuration and is identified as a glass modifier. Uranyl bonding is particularly sensitive to the types of neighboring cation and as a result provides a useful indicator in the glass of the corrosion processes taking place. The hydration and complexing of uranyl-like groups are observed as a function of corrosion treatment with the eventual generation of hydrated silicate groups at the surface. These sequential changes are well-described by the modified random network model for glass structure.

(63) Eden, M. In *Proceedings, 4th Berkeley Symposium on Mathematics and Statistical Problems*; Neyman, F., Ed.; University of California Press: Berkeley, CA, 1961; p 223.

Acknowledgment. This work was supported by the SERC and the European Commission. We would like to thank the Daresbury Laboratory for the provision of synchrotron radiation facilities. Useful discussions on the leaching process and the structural chemistry of uranium are acknowledged with F. Lanza, E. Towns-Andrews, and K. Bagnall. Sadly, both Richard Thornley and Marcello Antonini died in separate tragedies before the completion of this work. Their enthusiasm for synchrotron radiation and solid-state science was immense. This paper is dedicated unreservedly to their memory.

Registry No. U, 7440-61-1.

Technetium Complexes of 3,5-Di-*tert*-butylcatechol. Direct Synthesis of Tris(3,5-di-*tert*-butylcatecholato)technetium(VI) and Bis(3,5-di-*tert*-butylcatecholato)-(di-*tert*-butylamidophenolato)technetium(VI) from Ammonium Pertechnetate

Lynn A. deLearie, R. Curtis Haltiwanger, and Cortlandt G. Pierpont*

Contr ution from the Department of Chemistry and Biochemistry, University of Colorado, Boulder, Colorado 80309. *Received August 29, 1988*

Abstract: The reaction between 3,5-di-*tert*-butylcatechol and ammonium pertechnetate in methanol produces a mixture of tris(3,5-di-*tert*-butylcatecholato)technetium(VI) ($Tc(DBCat)_3$) and bis(3,5-di-*tert*-butylcatecholato)(di-*tert*-butylamidophenolato)technetium(VI) ($Tc(DBCat)_2(DBAP)$). The amidophenolate ligand of $Tc(DBCat)_2(DBAP)$ appears to result from Schiff-base condensation of ammonia from ammonium ion with catechol. When the reaction is carried out in the presence of excess 3,5-di-*tert*-butylcatechol only small quantities of $Tc(DBCat)_2(DBAP)$ are formed. Crystallographic characterization of $Tc(DBCat)_3$ has shown that the molecule crystallizes in the monoclinic space group $P2_1/n$ in a unit cell of dimensions a = 15.892 (3) Å, b = 15.878 (4) Å, c = 16.367 (3) Å, β = 93.13 (1)°, and V = 4123 (1) Å^3. The complex molecule is of C_3 symmetry and the average ligand C–O bond length of 1.334 (13) Å is typical of values found for catecholate ligands. As such, the complex is a unique example of Tc(VI). Both $Tc(DBCat)_3$ and $Tc(DBCat)_2(DBAP)$ exhibit well-resolved 10-line EPR spectra in solution at room temperature. Coupling to the ^{99}Tc nucleus ($I = {}^9/_2$) of approximately 140 G is consistent with the d^1 Tc(VI) formulation for both complexes. They each undergo reversible one-electron oxidations to cationic complexes with surprising ease, and they each undergo two reversible one-electron reductions to Tc(V) and Tc(IV) forms of the complexes.

Technetium radiopharmaceuticals are becoming routinely used as anatomical imaging agents in nuclear medicine.[1] Two general approaches have been used in the development of tissue-specific imaging agents. Technetium-labeled molecules of defined biodistribution (i.e., antibodies) have been considered for use with the assumption that the in vivo distribution of the technetium-labeled species remains the same as that of the unlabeled carrier. A second approach has involved use of technetium coordination compounds, where biodistribution is controlled by the physical properties of the complex. These relationships are poorly understood, and the development of metal complex radiopharmaceuticals has been largely empirical.

The coordination chemistry of technetium has expanded dramatically over the past 5 years in conjunction with this interest. Clinical applications utilize the metastable ^{99m}Tc isotope in imaging experiments as a high-energy γ emitter with a relatively short $t_{1/2}$ (6.02 h). Inexpensive generators are available that conveniently produce $^{99m}TcO_4^-$ by the β decay of ^{99}Mo in $^{99}MoO_4^{2-}$. Developmental studies are frequently carried out on complexes of ^{99}Tc, which is a longer lived β emitter ($t_{1/2} = 2.1 \times 10^5$ years) and less difficult to handle in routine laboratory work. Synthetic procedures often require a prereduction of pertechnetate with Sn(II) or $Na_2S_2O_4$ prior to complex formation. Products of these reactions generally contain either Tc(III) or the $[Tc^VO]^{3+}$ core, by far the most common forms of the metal.

We now describe the products of the reaction between ammonium pertechnetate and 3,5-di-*tert*-butylcatechol. In this reaction, catechol serves as both a reducing agent and a chelating ligand in the formation of the tris(catecholato)technetium(VI) product. Additionally, the +6 charge of the metal is the least common oxidation state for technetium.

Experimental Section

$NH_4{}^{99}TcO_4$ was obtained from Oak Ridge National Laboratory and was recrystallized from water prior to use. 3,5-Di-*tert*-butylcatechol and 3,5-di-*tert*-butyl-1,2-benzoquinone were obtained from Aldrich Chemical Co., $Re_2(CO)_{10}$ and $KReO_4$ were obtained from Stream Chemical Co., and all were used as received. ^{99}Tc is a β emitter, and all manipulations were carried out in a well-ventilated fume hood by personnel wearing protective coats and gloves.

Synthesis of $Tc(DBCat)_3$ and $Tc(DBCat)_2(DBAP)$. $NH_4{}^{99}TcO_4$ (0.59 g, 3.31 mmol) and 3,5-di-*tert*-butylcatechol (2.34 g, 10.53 mmol) were dissolved in 80 mL of anhydrous methanol. The resulting solution was freeze–thaw–degassed once under Ar and refluxed for 24 h. The solid product obtained after complete evaporation of the reaction solution was washed with several aliquots of cold methanol. Product separation was achieved by column chromatography using a toluene mobile phase and silica gel as the solid support. Crystals of $Tc(DBCat)_3$ suitable for X-ray crystallography were grown directly from the reaction.

Synthesis of $Re(DBCat)_3$. $Re(DBCat)_3$ was synthesized from $Re_2(CO)_{10}$ and 3,5-di-*tert*-butylbenzoquinone by procedures described previously[2] or by the method below: $KReO_4$ (0.47 g, 1.64 mmol) and 3,5-di-*tert*-butylcatechol (1.09 g, 4.91 mmol) were freeze–thaw–degassed for

(1) (a) *Technetium in Chemistry and Nuclear Medicine*; Deutsch, E.; Nicolini, M.; Wagner, H. N., Jr., Eds.; Cortina International Verona: Verona, Italy, 1983. (b) Pinkerton, T. C.; Desilets, C. P.; Hoch, D. J.; Mikelsons, M. V.; Wilson, G. M. *J. Chem. Educ.* **1985**, *62*, 965. (c) Deutsch, E.; Libson, K.; Jurisson, S.; Lindoy, L. F. *Prog. Inorg. Chem.* **1983**, *30*, 75.

(2) deLearie, L. A.; Haltiwanger, R. C.; Pierpont, C. G. *Inorg. Chem.* **1987**, *26*, 817.

0002-7863/89/1511-4324$01.50/0